

Parallel Computation of Forced Vibration for A Compressor Cascade

Zongjun Hu* and Gecheng Zha[†]

Abstract

The forced vibration of the 2D NASA flutter compressor cascade is numerically simulated in full scale with parallel computation technique. The compressor cascade consists of 9 blades bounded by 2 wind tunnel side walls. The implicit line Gauss-Seidel iteration with dual time stepping is employed. The turbulence is modeled with the Baldwin-Lomax model. A newly developed high resolution efficient scheme, Zha-CUSP2 scheme, is applied to compute the inviscid flux. The blades vibrate with a constant inter blade phase angle of 180 degree. The numerical simulation is carried out at a zero degree incidence with reduced frequencies of 0.4, 0.8 and 1.2. The computed unsteady pressure, aerodynamic moment and the local stability are compared with the experiment measurement.

1 Introduction

Flutter in axial turbomachines is a highly undesirable and dangerous self-excited blade oscillation mode that can result in high cycle fatigue blade failure. Modern turbine engines employ transonic fan stages with high aspect ratio blades that are prone to flutter. It is important to understand the origins of flutter for reliable and safe operation of these engines.

Because flutter is a complicated nonlinear flow-structure interaction problem, the often used linearized methods are not able to capture the strong viscous effects, such as the shock-boundary layer interaction and flow separations. An accurate solver based on the time dependent fully nonlinear Navier-Stokes equations is highly desirable. However, solving the fully nonlinear Navier-Stokes equations is time consuming and it becomes more difficult when all the blades are vibrating in a full annulus. An often used method in studying the oscillating cascade is the phase-shifted periodic boundary condition. This method solves a single passage by applying a 'direct store' method[5] on its periodic boundaries. However it assumes that the blades harmonically oscillate with a constant inter blade phase angle (IBPA) and will not be able to handle more complicated conditions if the flow pattern varies across flow passages. For example, stall flutter usually does not have periodicity and no constant IBPA exists. A more rigorous way is to calculate all the passages together with full annulus and make the time marching synchronously.

The objective of this paper is to develop an efficient time dependent Navier-Stokes solver to calculate the fluid-structure interaction of multi-blade passages using the parallel computation technique. The NASA flutter cascade under investigation has 9 blades with wind tunnel walls. The blades vibrate with a constant IBPA[2]. The periodic condition is not needed in the full scale simulation. This is the first step toward the full annulus 3D turbomachinery computation of fluid-structure interaction. A new E-CUSP upwind scheme developed by Zha et al.[16, 17, 7] is applied in the solver for its accuracy and efficiency. The strategy used in this paper is more rigorous than that used in reference [14] to include the wind tunnel end wall, which plays an important role in the temporal and space periodicity in the cascade experiment[3].

The present 3D Navier-Stokes solver has been successfully applied to 3D steady and unsteady studies with and without flow separation phenomenon[9][8]. Parallel computation is implemented in this solver to simulate the multiple passages simultaneously.

*PhD Student, Email: zongjunhu@yahoo.com

[†]Associate Professor, Director of CFD & Aerodynamics Lab, Email: zha@apollo.eng.miami.edu

2 Governing Equations

The governing equations are the time dependent compressible Navier-Stokes equations. After normalization, the Navier-Stokes equations are written in general coordinates as the following,

$$\frac{\partial \mathbf{Q}}{\partial t} + \frac{\partial \mathbf{E}}{\partial \xi} + \frac{\partial \mathbf{F}}{\partial \eta} + \frac{\partial \mathbf{G}}{\partial \zeta} = \frac{1}{\text{Re}} \left(\frac{\partial \mathbf{R}}{\partial \xi} + \frac{\partial \mathbf{S}}{\partial \eta} + \frac{\partial \mathbf{T}}{\partial \zeta} \right) + \mathbf{D} \quad (1)$$

The equations is normalized based on the free stream variables, velocity U_∞ , density ρ_∞ , viscosity μ_∞ and temperature T_∞ . In Equation (1), \mathbf{Q} is the vector of conservative variables,

$$\mathbf{Q} = \frac{1}{J} \begin{bmatrix} \rho \\ \rho U \\ \rho V \\ \rho W \\ \rho E \end{bmatrix} \quad (2)$$

\mathbf{E} , \mathbf{F} and \mathbf{G} are the inviscid fluxes in ξ , η and ζ direction,

$$\mathbf{E} = \frac{1}{J} \begin{bmatrix} \rho U \\ \rho uU + \xi_x p \\ \rho vU + \xi_y p \\ \rho wU + \xi_z p \\ (\rho E + p)U \end{bmatrix}, \mathbf{F} = \frac{1}{J} \begin{bmatrix} \rho V \\ \rho uV + \eta_x p \\ \rho vV + \eta_y p \\ \rho wV + \eta_z p \\ (\rho E + p)V \end{bmatrix}, \mathbf{G} = \frac{1}{J} \begin{bmatrix} \rho W \\ \rho uW + \zeta_x p \\ \rho vW + \zeta_y p \\ \rho wW + \zeta_z p \\ (\rho E + p)W \end{bmatrix} \quad (3)$$

\mathbf{R} , \mathbf{S} and \mathbf{T} are the viscous fluxes in ξ , η and ζ direction respectively,

$$\mathbf{R} = \frac{1}{J} \begin{bmatrix} 0 \\ \xi_k \tau_{xk} \\ \xi_k \tau_{yk} \\ \xi_k \tau_{zk} \\ \xi_k \beta_k \end{bmatrix}, \mathbf{S} = \frac{1}{J} \begin{bmatrix} 0 \\ \eta_k \tau_{xk} \\ \eta_k \tau_{yk} \\ \eta_k \tau_{zk} \\ \eta_k \beta_k \end{bmatrix}, \mathbf{T} = \frac{1}{J} \begin{bmatrix} 0 \\ \zeta_k \tau_{xk} \\ \zeta_k \tau_{yk} \\ \zeta_k \tau_{zk} \\ \zeta_k \beta_k \end{bmatrix} \quad (4)$$

\mathbf{D} is an additional term due to the geometric conservation law[4]. This term is theoretically equal to zero but numerically still remains.

$$\mathbf{D} = \mathbf{Q} \left[\frac{\partial J^{-1}}{\partial t} + \left(\frac{\xi}{J} \right)_\xi + \left(\frac{\eta}{J} \right)_\eta + \left(\frac{\zeta}{J} \right)_\zeta \right] \quad (5)$$

In the above equations, ρ , u , v , w and p are the density, velocity components in x , y and z direction and the static pressure. $J = \partial(\xi, \eta, \zeta) / \partial(x, y, z)$ is the coordinates transformation Jacobian matrix. E is the total energy per unit mass and is determined by

$$E = \frac{p}{\rho(\gamma-1)} + \frac{1}{2} (u^2 + v^2 + w^2) \quad (6)$$

U , V and W are the contravariant velocities in ξ , η and ζ direction respectively:

$$U = \xi_t + \xi_x u + \xi_y v + \xi_z w \quad (7)$$

$$V = \eta_t + \eta_x u + \eta_y v + \eta_z w \quad (8)$$

$$W = \zeta_t + \zeta_x u + \zeta_y v + \zeta_z w \quad (9)$$

β_k is expressed as the following,

$$\beta_k = u\tau_{kx} + v\tau_{ky} + w\tau_{kz} - q_k \quad (10)$$

where q_k is the heat flux in $k = x, y, z$ direction.

The stress τ_{ij} is composed of the laminar part and the turbulent part. Both parts are determined by the main stream flow gradient and the corresponding laminar or turbulent viscosity. The molecular viscosity is computed

by the Sutherland's law and the turbulent viscosity is computed using a two layer algebraic eddy viscosity model, Baldwin-Lomax turbulence model[1]. The grid is specially treated in the near wall region to achieve the orthogonality requirement of the turbulence model. The thermal transport coefficients for the heat fluxes in the laminar and turbulent parts in the energy equation are determined by a laminar and a turbulent Prandtl number.

3 Numerical Methods

The governing equation (1) is solved with a finite volume technique and discretized in a node-centered form. On the control volume interface, the inviscid fluxes are computed by the Zha-CUPS2 scheme[15]. Zha-CUPS2 scheme is a E-CUSP scheme and the inviscid flux is split into convective and pressure vectors with the total energy included in the convective part. This scheme has very low numerical dissipation. This scheme is consistent with characteristics disturbance propagation direction and thus the high numerical stability and robustness are achieved. The Zha-CUPS2 scheme is also efficient in CPU usage because it only uses scalar dissipation instead of the matrix dissipation used by schemes such as the Roe scheme[13]. The third order accuracy for the inviscid fluxes is employed with the MUSCL extrapolation of van Leer[11]. The viscous fluxes are computed using the second order central differencing. The final accuracy order in space is hence 2nd order.

3.1 Time marching scheme

The time marching of the time dependent governing equations (1) uses the technique of dual time stepping suggested by Jameson[10]. A pseudo temporal term $\frac{\partial \mathbf{Q}}{\partial \tau}$ is added at the left hand side of the governing equations (1) and the updated equations are solved implicitly using the line Gauss-Seidel iteration method. Within each physical time step, iterations are carried out with the pseudo time until it is converged. The local time step technique is applied to accelerate the convergence within each physical time step Δt . Because the pseudo temporal term vanishes at the end of each physical time step, it will not affect the accuracy of the solution. The physical temporal term $\frac{\partial \mathbf{Q}}{\partial t}$ is discretized implicitly using the following second order backward three point differencing scheme,

$$\frac{\partial \mathbf{Q}}{\partial t} = \frac{3\mathbf{Q}^{n+1} - 4\mathbf{Q}^n + \mathbf{Q}^{n-1}}{2\Delta t} \quad (11)$$

where $n-1$, n and $n+1$ are sequential physical time level indexes. The pseudo temporal term $\frac{\partial \mathbf{Q}}{\partial \tau}$ is discretized implicitly using the first order Euler scheme on the pseudo time index m and $m+1$ within each physical time interval Δt . The discretized governing equations are then written as the following,

$$\begin{aligned} & \left[\left(\frac{1}{\Delta \tau} + \frac{1.5}{\Delta t} \right) I - \left(\frac{\partial \mathbf{RHS}}{\partial \mathbf{Q}} \right)^{n+1,m} \right] \delta \mathbf{Q}^{n+1,m+1} \\ & = \mathbf{RHS}^{n+1,m} - \frac{3\mathbf{Q}^{n+1,m} - 4\mathbf{Q}^n + \mathbf{Q}^{n-1}}{2\Delta t} \end{aligned} \quad (12)$$

where I is the identity matrix, \mathbf{RHS} is the net flux going through the control volume,

$$\mathbf{RHS} = -\frac{1}{V} \int_s \left[(E-R) \mathbf{e}_\xi + (F-S) \mathbf{e}_\eta + (G-T) \mathbf{e}_\zeta \right] \cdot \mathbf{ds} + \mathbf{D} \quad (13)$$

where \mathbf{s} is the control volume surface vector, \mathbf{e}_ξ , \mathbf{e}_η and \mathbf{e}_ζ are the unit vector in ξ , η and ζ direction, V is the volume of mesh cell.

Within each pseudo time interval, the Gauss-Seidel iteration is swept line by line on each direction back and forth once. The updated variables of the previous neighboring line are used immediately during the sweep as the Gauss-Seidel iteration requires. The dual time stepping technique also has the advantage to facilitate information exchange across the partitioned domain boundaries for parallel computation using implicit solver. The precise implicit treatment at the partitioned domain boundaries is not required as long as the solution is converged within each physical time step.

3.2 Parallel computation

Multiple blade passages are computed in the vibrating cascade unsteady simulation. The computation domain is split into a series of parallel passages roughly following the stream lines. The flowfields in the subdomains marches in time synchronously with the technique of parallel computation. The current study is carried out in a Beowulf computer system, which consists of a cluster of dual CPU Dell workstations. Each machine is equipped with two 2.8GHz CPUs and a shared memory of 2G. All computers share the same home directory, where the executable code and the input and output data are saved. The parallel computing CFD solver is implemented using the protocol of message passing interface (MPI). During the simulation, each subdomain is assigned to a single CPU process. All subdomains are solved simultaneously. After each pseudo time iteration, the information of two halo layers of flow variables and grids at a boundary between two physical neighboring subdomains are exchanged using MPI. The solution for each physical time step is considered to be converged when the maximum residual reaches the convergence criteria on all subdomains. One of the CPUs works as the master for the parallel computation system, which determines physical time step and controls the activities of all involved CPUs.

3.3 Moving grid system

To give even load for each CPU, the mesh in each subdomain has the same size. The mesh is H-type and is generated by solving the elliptic Possion equation. Because of the high stagger angle of the cascade, the grid lines are highly twisted. As suggested in reference[6], a boundary layer mesh is generated in the vicinity of the blade wall surface using algebraic method. The grid lines are made either parallel or normal to the solid wall. This is preferred by the Baldwin-Lomax model, in which the search of f_{\max} and y_{\max} following a line normal to the wall is required.

When the blades vibrate at a prescribed frequency, the mesh for each subdomain moves accordingly. The boundary mesh layer is fixed to the wall surface and moves with the blade. The inner mesh has to be recalculated by solving the elliptic Possion equation which is a time consuming process. The blades in the current study vibrate harmonically. The meshes hence also vary harmonically and are repeated after each vibration cycle. The mesh generation time is reduced by saving a series of meshes in a vibration cycle in advance and reusing them in the following vibration cycles. To save the storage, meshes in 20 uniform time intervals are generated before the simulation starts. The meshes at any time level during the vibration are linearly interpolated using the previously-generated meshes for all subdomains.

3.4 Boundary conditions

The boundary conditions involved in the simulation are the inlet, outlet, wall and MPI interface boundaries as shown in Fig. 1. The flow at inlet is subsonic, thus the total pressure, total temperature and the flow angles are fixed at the inlet boundary. The static pressure is extrapolated from the inner domain. The flow at the outlet is also subsonic. The static pressure is specified at the outlet and all other variables are extrapolated from the inner domain. For the MPI interface boundaries, two halo layers of mesh and flow variables are saved and exchanged between the two neighboring subdomains after each pseudo time step via MPI.

At the moving boundary surface, the no-slip boundary condition is enforced by extrapolating the velocity between the phantom cells and the inner cells. Take u as example,

$$u_o = 2u_w - u_i \quad (14)$$

where u_o and u_i denote the velocity at the phantom cell and the first inner cell, u_w is the velocity of the moving wall surface. Two other conditions for temperature and pressure are also imposed on the solid wall. Take the lower wall in η direction as example, the wall is treated as adiabatic and the temperature at the phantom cell is determined by

$$\frac{\partial T}{\partial \eta} = 0 \quad (15)$$

The inviscid normal momentum equation is used to calculate the pressure at the phantom cell as the following[12],

$$\frac{\partial p}{\partial \eta} = - \left(\frac{\rho}{\eta_x^2 + \eta_y^2} \right) (\eta_x \dot{u}_w + \eta_y \dot{v}_w) \quad (16)$$

where \dot{u}_w and \dot{v}_w are the accelerations of the moving grid.

3.5 Parameters used in flow analysis

The steady state static pressure coefficient is defined as the following,

$$C_p(x/c) = \frac{p(x/c) - p_\infty}{\frac{1}{2}\rho_\infty U_\infty^2} \quad (17)$$

where p_∞ , ρ_∞ and U_∞ are the averaged pressure, density and velocity at inlet.

The blades vibrate harmonically with a constant IBPA. The motion of the n th blade is defined by the blade deflection angle[2],

$$\alpha^n(t) = \alpha_0 + \hat{\alpha} Re[\exp(i(\omega t + n\beta))] \quad (18)$$

where n is the blade index, t is the time, α_0 is the deflection angle at the mean blade position, $\hat{\alpha}$ is the amplitude of blade deflection, Re denotes the real part of a complex value, ω is the angular frequency, β is the inter blade phase angle.

The reduced frequency k_c is defined based on the chord length C as the following,

$$k_c = \frac{\omega C}{U_\infty} \quad (19)$$

The first harmonic unsteady pressure coefficient is defined as,

$$C_p(x) = \frac{p_1(x)}{\rho_\infty U_\infty^2 \hat{\alpha}} \quad (20)$$

where $p_1(x)$ is first harmonic pressure along the blade surface. It is a complex value obtained from the unsteady pressure signals using the Fourier transformation. $p_1(x)$ has a phase angle relative to the blade motion α .

The time dependent aerodynamic moment coefficient is defined as,

$$C_m(t) = \frac{-\int \mathbf{r} \times p(x) ds}{\frac{1}{2}\rho_\infty U_\infty^2 \hat{\alpha}} \quad (21)$$

where $p(x)$ is the unsteady pressure along the blade surface, \mathbf{s} is the surface area vector pointing outward from the blade, \mathbf{r} is the vector pointing from the pivot location to an arbitrary point x on the surface.

The imaginary part, or the out of phase part of the unsteady pressure determines the damping or excitation of the blade motion. The aerodynamic damping coefficient is defined as,

$$\Xi = -Im(C_m) \quad (22)$$

where Im denotes the imaginary part of a complex value. A positive Ξ corresponds to a damped oscillation.

4 Results and Discussions

The NASA Lewis Oscillating Cascade test section consists of 9 identical airfoils with the cross section similar to the tip airfoil of modern low-aspect ratio fan blades[2]. The airfoil has a chord of 8.89 cm and is installed with a stagger angle of 60°. The solidity is 1.52. In the experiment, the inlet Mach number is 0.5. All blades vibrate simultaneously along a pitching axis at 0.5 chord with a constant IBPA of 180°. The oscillating amplitude is 1.2° and the reduced frequency based on chord varies at 0.4, 0.8 and 1.2. The blade motion is identical on every other blade. The two neighboring blades always vibrate in opposite direction.

The inlet Mach number $Ma = 0.5$ is achieved by adjusting the outlet static pressure level. The Reynolds number based on the chord length is 9×10^5 . The flow incidence is 0°. For the unsteady dual-time stepping, one physical blade oscillation cycle is divided into 100 time intervals and 100 pseudo time Gauss-Seidel iterations are carried out for each physical time step. The 100 pseudo time iterations are proved to be sufficient to obtain a converged solution within a physical time step with the residual reduced by 3 orders in magnitude. Before the unsteady simulation, the corresponding steady state calculation is carried out to obtain the initial flow field for the unsteady computation.

The inlet flow angle is adjusted to 61° to obtain good agreement with the steady state experimental surface pressure distribution.

Before the full scale computation, a simplified 2-passage cascade is computed with a reduced frequency of $k_c = 0.8$ by applying the periodic boundary condition. The information of the moving mesh and the conservative variables are exchanged across the periodic boundary. The multi-passage full scale simulation is then conducted for the 9-blade cascade with the wind tunnel side walls for more realistic results. The periodic boundary condition is not needed. The vibration frequencies of $k_c=0.4, 0.8$ and 1.2 are calculated and compared with the experiment measurement. The influence of the end walls are studied by comparing the results of $k_c=0.8$ from both simulations.

4.1 Computation domain decomposition and mesh generation

As shown in Fig. 1, the computation domain which is consistent with the experiment configuration is split into 10 subdomains based on flow passages P1 through P10. The 10 subdomains are computed by 10 CPUs running in parallel. The subdomains are separated from their neighbors by the blade surfaces B1 through B9 and the MPI interface boundaries. The MPI interface boundaries are straight lines passing through the leading edge (LE) and trailing edge (TE) of the blades with appropriate angles in accord with the local flow direction. The pitchwise distance between the end wall and the blade is half of the inner pitch distance. The US (upper surface) is the suction surface and LS (lower surface) is the pressure surface.

The inlet and outlet boundaries are set as 1.5 and 3 times chord length away from the airfoil LE and TE in axial direction. A part of the mesh is shown in Fig. 2 with the regions of LE and TE zoomed in for more details. The H-type mesh is generated for each subdomain respectively. Each subdomain shares the grid point distribution on the common MPI interface boundaries with its neighbors. To achieve good orthogonality on the blade surface, an additional algebraic boundary layer mesh is generated in the wall surface region. As shown in Fig. 2, the grid lines are orthogonal on all blade surfaces except the small regions at LE and TE. The mesh size is $195(\xi) \times 180(\eta)$ for all subdomains. For clarity, the mesh is plotted every 4 lines in the un-zoomed plots. The blade surface has 100 points in streamwise direction. The boundary layer has 40 points in pitchwise direction. Because of the high gradient of the flow variables in near wall region, the mesh is clustered near the wall surfaces. On the blade surfaces, the grid points are also clustered toward the LE and the TE in streamwise direction.

4.2 Simulation in two passage cascade

The two passage cascade simulation uses the meshes of two inner neighboring passages (P2 and P3) in the compressor cascade. As shown in Fig. 3, The blade between the two passages is called BC (blade at center) and the two blade surfaces on the two outside periodic boundaries are treated as blade BP (blade at periodic boundary).

The steady state pressure coefficient distributions along the blade surfaces are plotted in Fig. 4. The pressure coefficient predicted agrees well with the measurement. The result on BC agrees very well with that of BP, which shows good periodicity is achieved on the pitchwise direction.

Fig. 5 shows the pressure variation history on two points on the suction surface (US) and the pressure surface (LS) respectively. The pressure on the suction surface is located at $x/C = 0.15$ and the pressure on the pressure surface is located at $x/C = 0.1$. The temporal periodicity is achieved very soon after the start of the vibration simulation. Because of the excellent temporal periodicity, the unsteady data extracted from a single blade motion cycle is enough for the unsteady Fourier analysis. The IBPA of 180° is clearly shown by comparing the pressure maximums and minimums on BC and BP.

The unsteady pressure coefficients are plotted in Fig. 6 and Fig. 7 for suction surface (US) and the pressure surface (LS) respectively. The unsteady pressure coefficient C_p is expressed in terms of the real part or in phase part and the imaginary part or out of phase part. On the suction surface, as shown in Fig. 6, the CFD results compare fairly well with experiment data after 30% chord. The real part of the coefficient is predicted lower than experiment data on leading edge, but the trend agrees very well with the experiment. The imaginary part is over predicted in the leading edge region. On the pressure surface, as shown in Fig. 7, the real part of the unsteady pressure coefficient agrees well with the experiment data. The imaginary part is under predicted compared with the measurement on the front part of the blade. This means that the CFD does not accurately capture the phase angle difference between the pressure response and the blade motion. A local flutter stability analysis based on the aerodynamic work per cycle suggested by Buffum[2] is presented in Fig. 8 by plotting $(0.5 - \frac{x}{c}) \text{Im} (C_{p,\text{upper}} - C_{p,\text{lower}})_{1\text{st}}$. The current numerical simulation predicts a larger local stable region on the front part of the blade. On the aft part, the experiment data indicates a

shallow stable region. The CFD predicts the trend very well. The aft part stable region is predicted more shallow than the experiment.

4.3 Simulation in full scale cascade

The full scale steady and unsteady simulation use the same inlet flow angle as that of the 2-passage case. In the steady state calculation, all blade are parallel to each other at their mean positions. As shown in Fig. 1, the end wall is made up of 3 sections, which have different angles relative to the x axis: $\alpha_1 = 61^\circ$, $\alpha_2 = 60^\circ$ and $\alpha_3 = 64^\circ$. The middle section is parallel to the blade at its mean position. The front and aft sections follow the inlet and outlet averaged flow directions obtained in the 2-passage steady state computation.

The steady state Mach number contours for the full scale cascade is shown in Fig. 9. The flow pattern is highly influenced by the end wall especially for the near end wall passages, P1 and P10. The influence is reduced rapidly from the boundary passages to the inner passages. Good periodicity in flow pattern is achieved among the inner passages (P3 through P8). Three center blades, B4, B5 and B6 are chosen to study the steady and unsteady periodicity in the rest of the paper. Even though the periodicity looks good in the Mach contour plot, the static pressure distribution still shows the influence of the end walls on different blades.

Fig. 10 shows the pressure coefficient chordwise distribution on the 3 center blades. The experiment measurement and the 2-passage calculation results are also plotted for comparison. The surface pressure increases gradually from B4 to B6 on both the pressure surface and the suction surface. The pressure distribution on blade B6 is closest to the 2-passage periodic results on most part of the surfaces. The experiment measurement also shows the pressure variation on different blades[2], but its variation trend is opposite to the current numerical results. A possible reason for this difference is that the inlet and outlet end wall angles used in the experiment may differ from the values used in the current simulation. The experimental angles are not available. Such a pitchwise flow pattern difference is also expected in the following unsteady calculations.

The full scale unsteady simulation is first carried out for a reduced frequency $k_c = 0.8$ to study the end wall influence on the periodicity of the blade unsteady characteristics. Figs. 11 and 12 are the unsteady pressure coefficient chordwise distribution on the 3 center blades compared with the 2-passage cascade and the experiment results. On the upper surface, as shown in Fig. 11, the 3 blades have very similar unsteady coefficients on most of the chordwise distance. The results of blade B6 are closest to those of the 2-passage calculation. The difference between the full scale results and the 2-passage results mainly locate at the front and center part of the blade. The full scale results agree with the experiment better in the center part. On the lower surface, as shown in Fig. 12, the full scale results of the 3 blades are similar. The 2-passage results are closer to the experiment data in the real part.

As shown in Fig. 13, the full scale calculations predict higher stability on the front part of the blade compared with the 2-passage results. The full scale results are closer to the experiment measurement on the aft part of the blade. In the chordwise region of $x/C = 0.5$ to $x/C=0.7$, the measured stability is better predicted in the full scale results. The 2-passage results shows instability in the same region. The end wall influence on the flow pattern periodicity is clearly shown in the unsteady aerodynamic moment oscillation plots within a whole blade motion cycle in Fig. 14. The moment is plotted versus the normalized deflection angle, $\alpha' = (\alpha - \alpha_0) / \hat{\alpha}$. Because of the end wall influence, the moment oscillations on the 3 center blades are different. They are also different from the 2-passage calculation results. The anti-clockwise direction of all the unsteady moment curves indicates negative work acted by the fluid on the blade. The blade motion is therefore damped down by the fluid flow. The blade motion is stable, which corresponds to a positive damping coefficient Ξ . The area enclosed by the moment curve indicates the magnitude of the work exchanged between the fluid and the blade, which is also proportional to the magnitude of the damping coefficient.

The damping coefficients on all the 9 blades in the full scale calculation versus the blade number are shown in Fig. 15. The damping coefficient varies among the blades. The damping coefficients for blade B4, B5 and B6 are 0.67, 0.65 and 0.68 respectively. Blade B1 has the lowest stability ($\Xi = 0.45$) and blade B9 has the highest stability ($\Xi = 1.4$). The damping coefficient distribution is more uniform on the center blades (B3 through B7), even though small variation exists. The blade stability in the full scale cascade depends on the location of the blade. The damping coefficient obtained in the 2-passage periodic computation is 0.55.

Fig. 16 plots a series of Mach number contours around blade B5 and B6. A separation bubble is generated and grows periodically on the leading edge of the suction surface. At $t = 0$, the two blades are initially located at their mean positions and are parallel to each other. Blade B5 then rotates in the counter-clockwise direction with a negative deflection angle (nose down). At the same time, blade B6 is rotating in the clockwise direction with a positive deflection angle (nose up). At $t=0.2T$, blade B5 is close to its minimum deflection position. The separation

bubble at its LE is pushed downstream and shrinks in size. At $t=0.4T$, blade B5 is rotating back from its minimum deflection location toward its mean position, the separation bubble disappears from the suction surface. At $t = 0.8T$, a new separation bubble is generated when blade B5 passes its maximum deflection position and rotates back toward its mean position. The bubble obtains its maximum size when the blade is close to its mean position. Similar phenomenon is observed on the neighboring blade B6, but with a phase difference of 180° .

More extensive unsteady simulations are carried out for reduced frequencies $k_c = 0.4$ and $k_c = 1.2$. Figs. 17 and 18 show the unsteady pressure coefficient chordwise distribution of $k_c = 1.2$. Similar to the results of $k_c = 0.8$, the predicted unsteady complex pressure coefficients are close to each other on the 3 center blades, even though some small difference exists. As shown in Fig. 17, on the upper surface, the imaginary parts of CFD results agree very well with the experiment results except that it is over-predicted in the region of $x/C=0.15$ to $x/C=0.40$. The real part is also predicted quite well on the middle and aft part of the blade. On the lower surface, as shown in Fig. 18, the predicted real parts compare very well with experiment. The Imaginary part is under-predicted from LE to $x/C = 0.7$.

The local stability analysis for $k_c = 1.2$ is plotted in Fig. 19. The correct trend is predicted compared with the experiment measurement, even though the magnitude does not agree very well. The stability is over-predicted in LE region. The unstable region predicted on the front part of the blade is smaller than the experiment results. The stability is predicted on the aft part, but the magnitude is smaller than the experiment data. The damping coefficients for all the blades are plotted in Fig. 20. The damping coefficients for blade B4, B5 and B6 are 0.81, 0.78 and 0.84 respectively. The stability increases with the frequency. Similar to the results of $k_c = 0.8$, the most stable blade is blade B9 ($\Xi=1.5$) and the least stable blade is blade B1 ($\Xi=0.6$). The damping coefficient is more uniformly distributed on the central blades. The variation of the damping coefficient on the center blades increases with the increasing frequency.

Because of the lack of experiment data, the unsteady pressure coefficient of $k_c=0.4$ is not presented for comparison. However, the local stability is analyzed and compared with the experiment data in Fig. 21. Similar to the results of $k_c = 0.8$ and $k_c = 1.2$, the trend is predicted well, but the magnitude differs from the experiment. As expected, the damping coefficient distribution is more uniform on center blades (Fig. 22). The variation of their magnitudes decreases with the decreasing vibration frequency compared with the high frequency cases of $k_c = 0.8$ and $k_c = 1.2$. The damping coefficients on blade B4, B5 and B6 are 0.448, 0.446 and 0.434 respectively. The most stable blade is B9 with $\Xi = 1.02$ and the least stable blade is B1 with $\Xi = 0.28$.

The unsteady aerodynamic moment oscillations on blade B5 under the 3 frequencies under investigation are plotted together and compared in Fig. 23. The damping coefficient increase with the increasing frequency is indicated by the increased area enclosed by the unsteady moment oscillation curve. The local stability analysis is summarized for all the 3 frequencies in Fig. 24. The computation results indicate higher stability near the leading edge for higher frequency vibration, which is consistent with the experiment measurement. Even though the destabilization region on the front part of the blade and the stability magnitude on the aft part of the blade predicted by the numerical computation are smaller than those in the experiment, the trend is predicted well. Both the destabilization and stabilization increase with the increasing frequency.

5 Conclusions

The fully nonlinear time dependent Navier-Stokes equations are solved with the parallel computation technique to simulate the unsteady flow field in a full scale compressor cascade with forced blade vibration. The calculation in this paper is conducted with a low incidence of 0° and a subsonic inflow $M=0.5$. The blade motion amplitude is 1.2° and the inter blade phase angle is 180° . The full scale computation is carried out for 3 reduced frequencies, 0.4, 0.8 and 1.2. The blade stability under different vibration frequency is analyzed. The end wall influence on the steady and unsteady flow characteristics is studied by comparing the full scale results with the 2-passage periodic cascade results at $k_c=0.8$. The conclusions are the following:

1. The flow pattern in the full scale cascade shows that the flowfield is affected by the existence of the end walls. The steady state blade surface pressure varies with the the blade position in the cascade. The periodicity of the flow pattern is improved by adjusting the end wall configuration. The end wall influence attenuates rapidly from boundary passages to center passages. Good periodicity is achieved in the inner passages. The full scale computation gives better results of the unsteady pressure coefficient, local stability and aerodynamic moment among the center blades.
2. All blades in the full scale cascade are stable, which is indicated by a positive damping coefficient. The damping

coefficient is more uniformly distributed on center blades. The most stable and the least stable blades are the two boundary blades. The damping coefficient and its variation across the center blades increase with the increasing vibration frequency.

3. The unsteady pressure coefficients are predicted well compared with the experiment measurement. The local stability trend is correctly predicted in the numerical computation. The blade local stability is over-predicted on LE and under-predicted on the aft part. The destabilization region located at the front part of the blade is predicted smaller compared with the experiment. The predicted stabilization and destabilization increase with the increasing frequency, so do the damping coefficients.

References

- [1] B. S. Baldwin and H. Lomax. Thin layer approximation and algebraic model for separated turbulent flows. *AIAA Paper 78-257*, 1978.
- [2] D. H. Buffum, V. R. Capece, A. J. King, and Y. M. EL-Aini. Oscillating cascade aerodynamics at large mean incidence. *Journal of Turbomachinery*, 120, 1998.
- [3] D. H. Buffum and S. Fleeter. Wind tunnel wall effects in a linear oscillating cascade. *Journal of Turbomachinery*, 115:147–156, 1993.
- [4] Xiangying Chen, Gecheng Zha, and Zongjun Hu. Numerical simulation of flow induced vibration based on fully coupled fluid-structural interactions. submitted to 34th AIAA Fluid Dynamics Conference, 2004.
- [5] J. I. Erdos, E. Alzner, and W. McNally. Numerical solution of periodic transonic flow through a fan stage. *AIAA Journal*, 15:1559–1568, 1977.
- [6] Björn Grüber and Volker Carstens. The impact of viscous effects on the aerodynamic damping of vibrating transonic compressor blades—a numerical study. *Journal of Turbomachinery*, 123, 2001.
- [7] Zongjun Hu and Gecheng Zha. Simulation of 3D flows of propulsion systems using an efficient low diffusion E-CUSP upwind scheme, July 2004. AIAA Paper 2004–4082, to appear in International Journal for Numerical Methods in Fluids.
- [8] Zongjun Hu, Gecheng Zha, and J. Lepicovsky. Numerical study of a cascade unsteady separation flow. GT2004-53195, June 2004.
- [9] Zongjun Hu, Gecheng Zha, and Jan Lepicovsky. Numerical study on flow separation of a transonic cascade, January 2004. AIAA Paper 2004–0199.
- [10] A. Jameson. Time Dependent Calculations Using Multigrid with Application to Unsteady Flows past Airfoils and Wings. AIAA Paper 91-1596, 1991.
- [11] B. Van Leer. Towards the ultimate conservative difference scheme, III. *Journal of Computational Physics*, 23:263–75, 1977.
- [12] S. A. Morton, R. B. Melville, and M. R. Visbal. Accuracy and Coupling Issues of Aeroelastic Navier-Stokes Solutions on Deforming Meshes. AIAA Paper-97-1085, 1997.
- [13] P. Roe. Approximate Riemann Solvers, Parameter Vectors, and Difference Schemes. *Journal of Computational Physics*, 43:357–372, 1981.
- [14] Stefna Weber and Max F. Platzer. A Navier-Stokes analysis of the stall flutter characteristics of the Buffum cascade. *Journal of Turbomachinery*, 122, 2000.
- [15] G.-C. Zha. Low Diffusion Efficient Upwind Scheme. *AIAA Journal*, 43, 2005.
- [16] G.-C. Zha and Z.-J. Hu. Calculation of Transonic Internal Flows Using an Efficient High Resolution Upwind Scheme. *AIAA Journal*, 42, No. 2:205–214, 2004.

[17] Gecheng Zha. A low diffusion efficient E-CUSP upwind scheme for transonic flows. AIAA Paper 2004-2707, to appear in AIAA Journal, 2004.

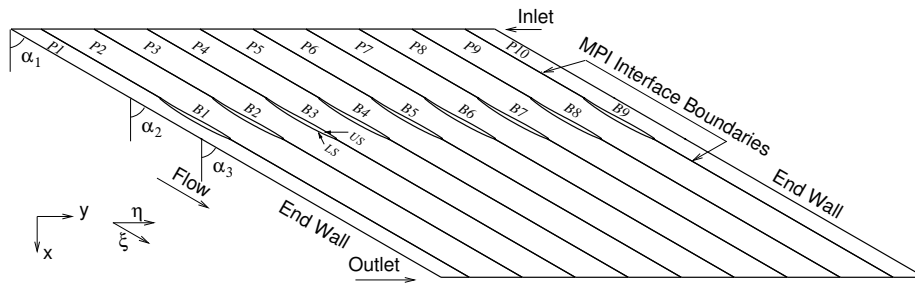


Figure 1: Computation Domain Configuration

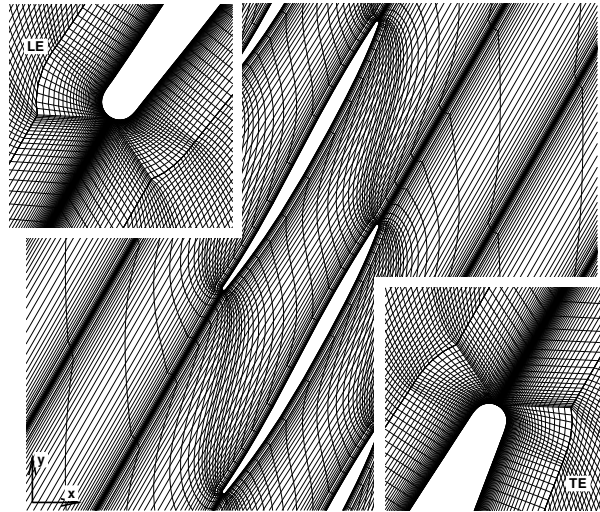


Figure 2: Computation mesh

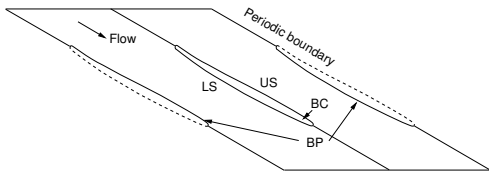


Figure 3: Two-passage cascade periodic computation domain

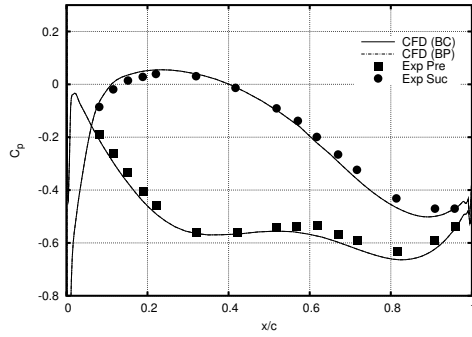


Figure 4: Steady state pressure coefficient in 2-passage cascade

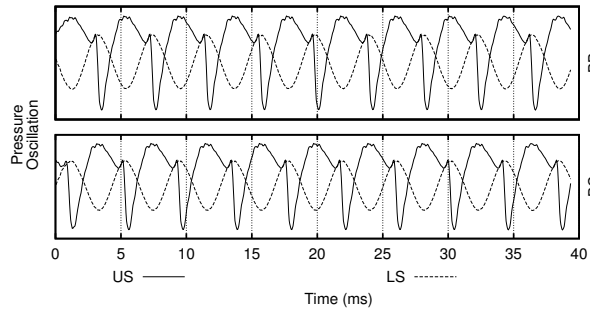


Figure 5: Pressure oscillation history, $k_c=0.8$

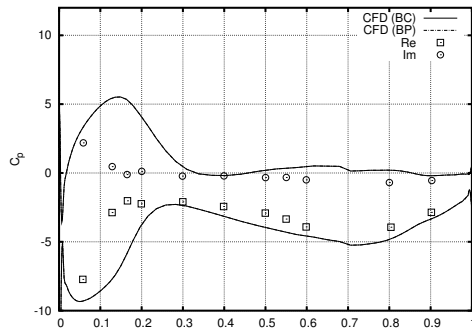


Figure 6: Unsteady pressure coefficient on upper surface in 2-passage cascade, $k_c = 0.8$

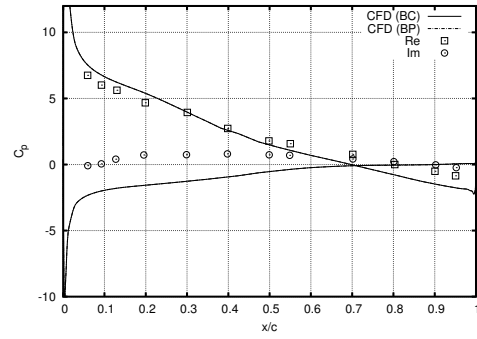


Figure 7: Unsteady pressure coefficient on lower surface in 2-passage cascade, $k_c=0.8$

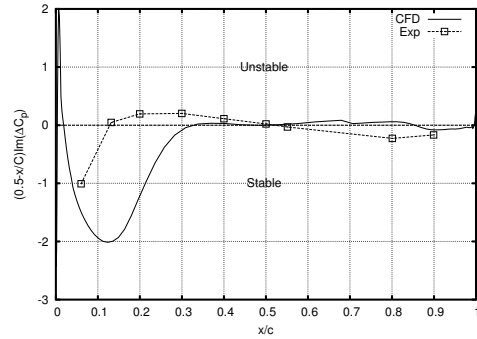


Figure 8: Local stability analysis in 2-passage cascade, $k_c=0.8$

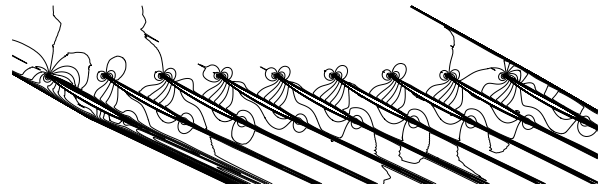


Figure 9: Steady state Mach contours in full scale cascade

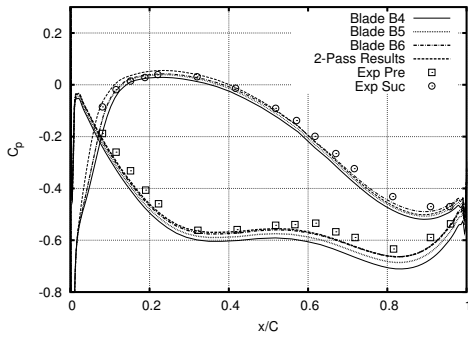


Figure 10: Steady state pressure coefficient in full scale cascade

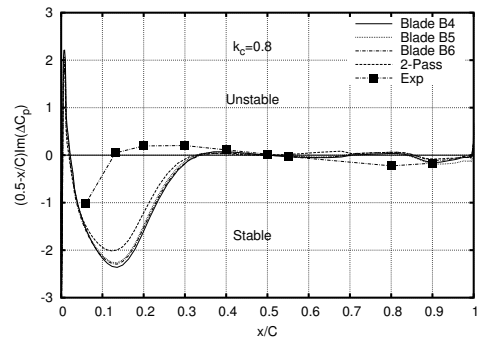


Figure 13: Local stability analysis, $k_c = 0.8$

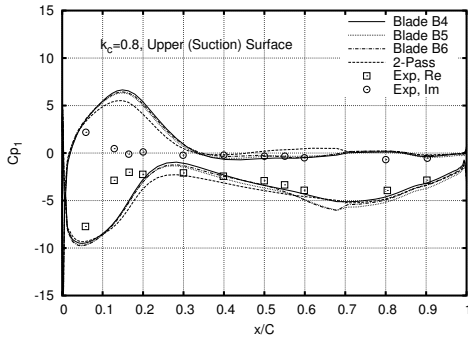


Figure 11: Unsteady state pressure coefficient on upper surface, $k_c = 0.8$

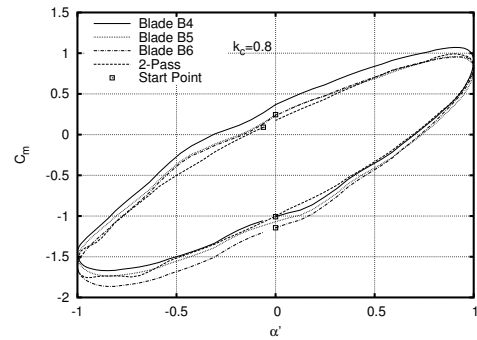


Figure 14: Unsteady aerodynamic moment oscillation, $k_c = 0.8$

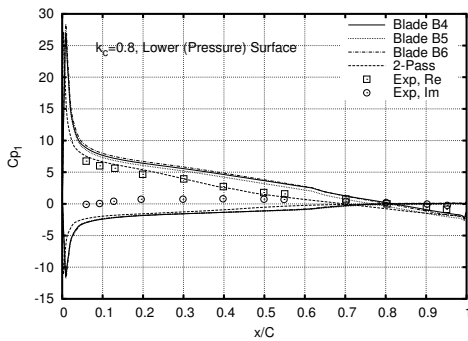


Figure 12: Unsteady state pressure coefficient on lower surface, $k_c = 0.8$

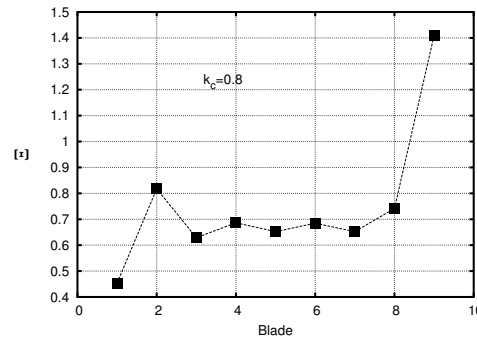


Figure 15: Damping coefficient distribution, $k_c = 0.8$

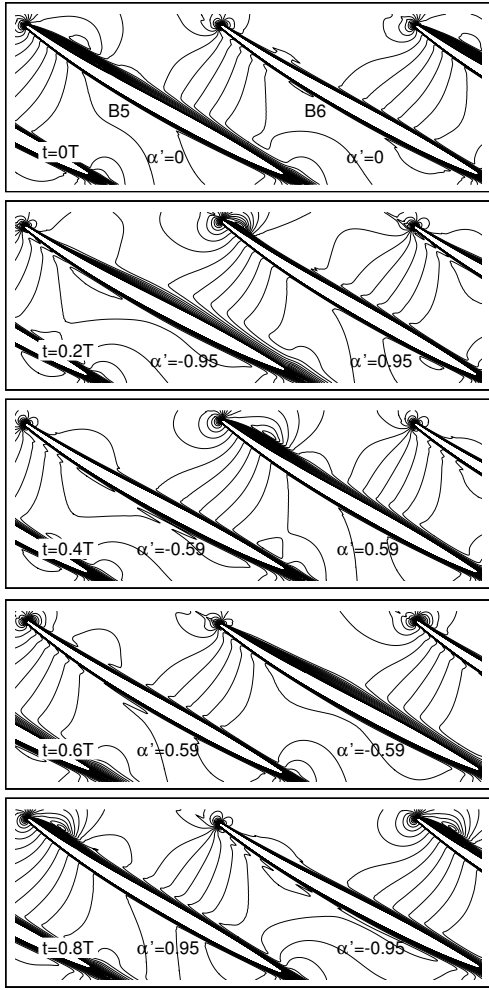


Figure 16: Unsteady Mach number contours, $k_c = 0.8$

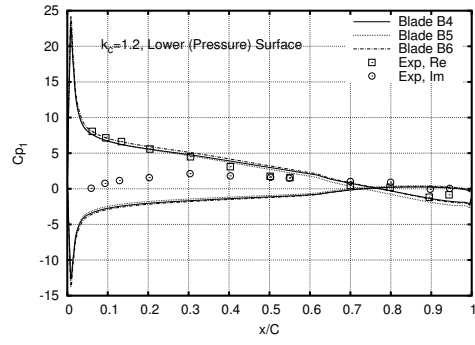


Figure 18: Unsteady pressure coefficient on lower cascade, $k_c = 1.2$

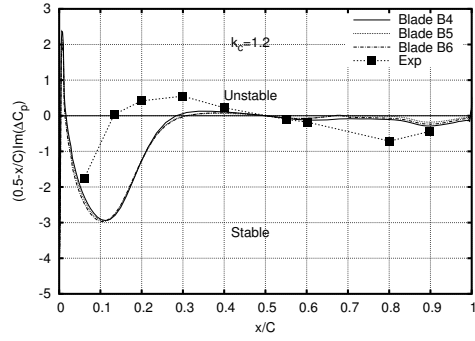


Figure 19: Local stability analysis, $k_c = 1.2$

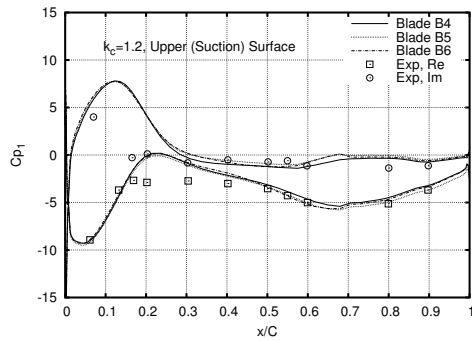


Figure 17: Unsteady pressure coefficient on upper surface, $k_c = 1.2$

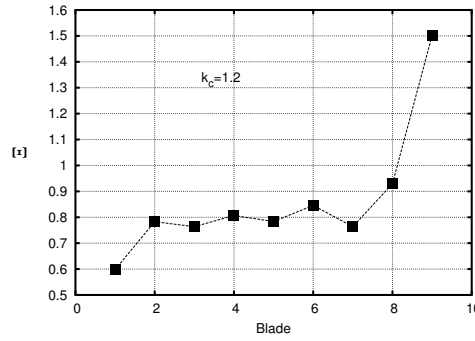


Figure 20: Damping coefficient distribution, $k_c = 1.2$

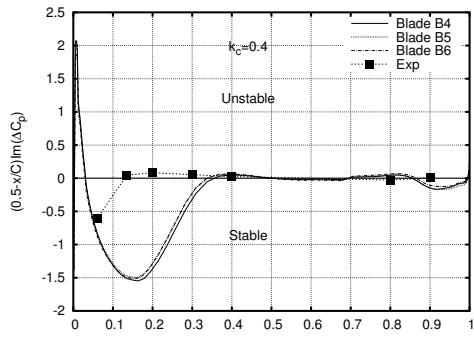


Figure 21: Local stability analysis, $k_c = 0.4$

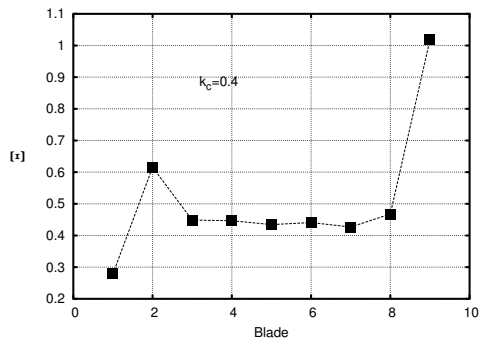


Figure 22: Damping coefficient distribution, $k_c = 0.4$

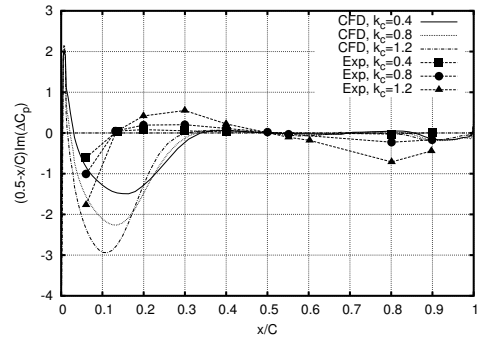


Figure 24: Local stability analysis comparison

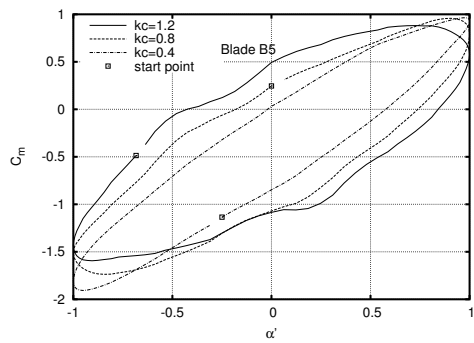


Figure 23: Unsteady aerodynamic moment oscillation comparison